SCIENTIFIC REPORTS

OPEN

SUBJECT AREAS:
ELECTRONIC PROPERTIES AND MATERIALS
TOPOLOGICAL INSULATORS
ELECTRONIC STRUCTURE

Received
15 May 2014

Accepted
27 August 2014

Published
30 September 2014

Correspondence and requests for materials should be addressed to J.F. (jfeng11@pku.edu.cn)

* Current address: Department of Physics, University of Texas at Austin, Austin, TX 78712, USA.

Superlattice valley engineering for designer topological insulators

Xiao Li[1,2]*, Fan Zhang[3], Qian Niu[1,2,4] & Ji Feng[1,2]

[1]International Center for Quantum Materials, School of Physics, Peking University, Beijing 100871, China, [2]Collaborative Innovation Center of Quantum Matter, Beijing, P. R. China, [3]Department of Physics, University of Texas at Dallas, Richardson, TX 75080 USA, [4]Department of Physics, University of Texas at Austin, Austin, TX 78712, USA.

A topological insulator is a novel state of quantum matter, characterized by symmetry-protected Dirac interfacial states within its bulk gap. Tremendous effort has been invested into the search for topological insulators. To date, the discovery of topological insulators has been largely limited to natural crystalline solids. Therefore, it is highly desirable to tailor-make various topological states of matter by design, starting with but a few accessible materials or elements. Here, we establish that valley-dependent dimerization of Dirac surface states can be exploited to induce topological quantum phase transitions, in a binary superlattice bearing symmetry-unrelated interfacial Dirac states. This mechanism leads to a rich phase diagram and allows for rational design of strong topological insulators, weak topological insulators, and topological crystalline insulators. Our ab initio simulations further demonstrate this mechanism in [111] and [110] superlattices of calcium and tin tellurides. While our results reveal a remarkable phase diagram for the binary superlattice, the mechanism is a general route to design various topological states.

A topological insulator (TI)[1–3] is an insulating material whose electronic Hamiltonian cannot be adiabatically deformed into that of an atomic insulator. Three primary types of TIs are known to occur in condensed matter materials, namely, strong and weak topological insulators (STI and WTI, respectively) protected by time-reversal symmetry[4,5], as well as topological crystalline insulators (TCI) protected by space group symmetry[6,7]. Characteristics of these TIs are gapless Dirac states on their interface with a normal insulator (e.g., vacuum). For STI and WTI, respectively, there are odd and even numbers of surface/interface Dirac points, according the $\mathcal{Z}_2$ classification scheme[4,5]. The SnTe material class is a representative TCI based on mirror symmetry, and is characterized by the existence of even number of surface states on high-symmetry surfaces. These symmetry-protected Dirac interfacial states give rise to the robust quantum transport, and offer promising routes to novel devices with potential applications in energy-efficient electronics and topological quantum computing. Therefore, the conceptual importance and application potential greatly promote the search of TIs[1–8].

However, the discovery of various TI phases relies on the natural crystalline solids to a great extent. It is highly desirable to be able to design various topological phases based on basic principle and available materials growth techniques. In particular, although one WTI has been experimentally synthesized, its surface states were not accessible to experimental probes[9]. Artificially created superlattices provide a natural arena for this endeavour, which is well provided with chemical, structural, orbital, and spin degrees of freedom. Indeed, the coupling of a TI surface state with a second material is especially intriguing. Proximity coupling the TI surface state to an *s*-wave superconductor breaks $U(1)$ gauge symmetry yielding a Majorana excitation[10]. A magnetic proximity effect can break time-reversal symmetry producing a chiral edge state[11,12]. It has recently been proposed that topological phases may emerge at the interfaces of oxide materials in two-dimensional quantum-well or thin film heterostructures[13–15]. In the present paper, we analyze the band topology in a three-dimensional binary superlattice with multiple symmetry-unrelated interfacial Dirac states. We show that various TIs can be rationally designed from valley-dependent interfacial-state dimerization. Using density-functional theory, we further demonstrate that a binary superlattice of calcium and tin tellurides can be fashioned into STI, WTI and TCI. In particular, the [110] superlattices of calcium and tin tellurides can host weak TI phases, which have topological surface states on the cleavage surface perpendicular to the [110] direction.

We begin with an intuitive picture of the interfacial state dimerization, analogous to the Su-Shrieffer-Heeger model of polyacetylene[16]. Consider a STI with a *single* Dirac point in its surface state per surface or interface. The idea is to grow a superlattice of alternating layers of the STI and a non-magnetic spacer normal insulator (NI), as shown in Fig. 1a. When the widths of parent and spacer layers are finite, there are two kinds of interlayer

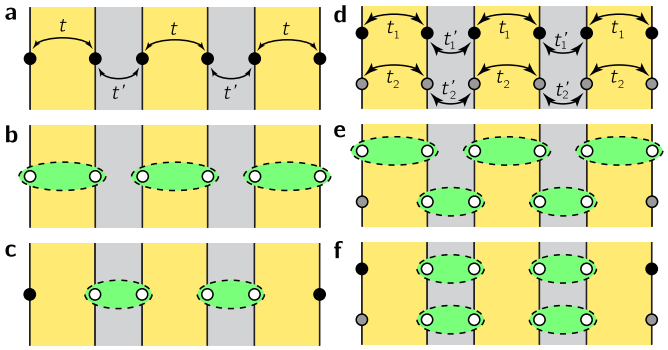

Figure 1 | Schematic depiction of surface-state dimerization. (a). A superlattice composed of the parent STI layers (yellow) and the spacer normal insulator layers (light grey). (b). Dimerization through the parent layers. (c). Dimerization through the spacer layers. (d). A superlattice with two independent Dirac interfacial states. (e). and (f). show two different schemes of dimerization. The black and gray circles represent isolated Dirac interfacial states while the white states are gapped because of dimerization, as indicated by the green blobs.

hoppings, t and t', between the Dirac interfacial states. They account for the covalent interactions between the pair of interfacial states, respectively, through the parent STI layer and through the spacer layer. There appears to be a delicate interplay between t and t'. In the limit of $t \gg t'$, the interfacial states dimerize through the parent TI layers, annihilating the Dirac nodes at finite truncation of the superlattice. In the opposite limit of $t \ll t'$, interfacial states dimerize through NI layers, and Dirac surface states are still present on outermost surfaces, leaving the superstructure a three-dimensional STI.

Now we consolidate the above dimerization picture in an effective Hamiltonian to describe the low-energy electronic states of the superlattice. Before introducing the interlayer couplings (t, t'), we describe a single Dirac interfacial state with a generic Dirac Hamiltonian, $H_v(\boldsymbol{k}) = c_v \boldsymbol{q}_v \cdot \sigma$, where $\boldsymbol{q}_v = (\boldsymbol{k} - \boldsymbol{k}_v)_{||}$ is the crystal momentum parallel to the cleaved surface, c_v is the Fermi velocity, and $\boldsymbol{\sigma}$ are the Pauli matrices of spin or pseudospin. We include an index v in $H_v(\boldsymbol{k})$, in anticipation of multiple Dirac valleys on one interface. Taking the direction perpendicular to the interfaces of the superlattice to be the z-direction and using the interfacial states, $|u\uparrow\rangle$, $|u\downarrow\rangle$, $|l\uparrow\rangle$, and $|l\downarrow\rangle$ as bases, the bulk electronic structure of the superlattice is determined by

$$\mathcal{H}_v(\boldsymbol{k}) = E_v + \tau_z H_v + \tau_x(t_v + t'_v \cos k_z) + \tau_y t'_v \sin k_z, \qquad (1)$$

where $\tau_z = \pm$ denote the upper (u) and lower (l) interfaces of a TI layer, $\uparrow$ and $\downarrow$ denote the two components of the spin or pseudospin and E_v reflects the possible particle-hole asymmetry of the TI. We have assumed that the superlattice possesses an inversion symmetry for simplicity, i.e., $|u\rangle$ and $|l\rangle$ are related by a space inversion operation $\hat{\mathcal{P}} = \tau_x$. Notice that when there is only a single valley, the model reduces to that of Burkov and Balents, who considered a magnetically doped superlattice of a STI with a normal insulator spacer for achieving Weyl semimetallic phases[17]. The band dispersion of Hamiltonian (1) reads $\varepsilon = E_v \pm \left(c_v^2 q_v^2 + t_v^2 + t_v'^2 + 2t_v t'_v \cos k_z\right)^{1/2}$, with a band gap $2\left||t_v| - |t'_v|\right|$. This band gap closes at $k_z = 0\ (\pi)$ when $t'_v = -(+)t_v$, which indicates topological quantum phase transitions. The topological classification depends on the relative strengths of $|t_v|$ and $|t'_v|$, leading to two possible surface-state dimerization schemes, in agreement with the limiting cases shown in Fig. 1b and c. Therefore, tuning $|t'_v/t_v|$ represents a continuous pathway to convert a nontrivial TI into a trivial NI.

When multiple Dirac interfacial states are present, the manifestation of interlayer coupling becomes more profound. An event of band inversion corresponds to a topological quantum phase transition, accompanied by the gap closure. Given that the surface states of the parent TIs are located at the time-reversal invariant (TRI) points in the $\boldsymbol{k}_{||}$-space of the superlattice, and the Hamiltonian (1) has inversion symmetry, it follows that for one of Dirac valley, v

$$\delta_v = \xi_v(0)\xi_v(\pi) = (-1)^{\Theta(|t'_v| - |t_v|)} \qquad (2)$$

determines the product of parity eigenvalues of the occupied bands at $k_z = 0$ and π. Here, $\Theta(x)$ is the Heaviside step function. When different surface states are not related by any symmetry, they may dimerize in distinct manners, as depicted in Fig. 1d. We can further conclude that the overall $\mathcal{Z}_2$ invariant is[5]

$$(-1)^{\nu_0} = \prod_v \delta_v. \qquad (3)$$

Here, the topological classification involves four $\mathcal{Z}_2$ numbers, ν_0; $(\nu_1\nu_2\nu_3)$. The overall topological index, ν_0, is the product of parity eigenvalues of all occupied states at all eight TRI points. When $\nu_0 = 1$, the system is a STI. When $\nu_0 = 0$, the three weak indices, ν_α ($\alpha = 1, 2, 3$), are computed, and when any or all of weak indices are non-zero it is said to be a WTI[5].

Based on the criteria in Eqs. (2) and (3), the opportunity to design various TI phases is immediately evident. If $|t_1| > |t'_1|$ and $|t_2| < |t'_2|$, the superlattice becomes a STI with $\nu_0 = 1$, as depicted in Fig. 1e. If $|t'_v/t_v| > 1$ for both interfacial states, a pair of Dirac nodes still persist on each outermost surface with $\nu_0 = 0$, as shown in Fig. 1f. The superlattice is either a WTI or a TCI. Here, WTI can be further characterized with three weak topological indices. Taking $\alpha = 3$ to be the z-direction, ν_1 is determined by values of δ's at $\boldsymbol{k}_{||} = (\pi, 0)$ and $\boldsymbol{k}_{||} = (\pi, \pi)$; that is, $(-1)^{\nu_1} = \delta(\pi,0)\delta(\pi,\pi)$. Similarly, $(-1)^{\nu_2} = \delta(0,\pi)\delta(\pi,\pi)$. Whereas ν_1 and ν_2 only depend on the relative magnitudes of $|t_v|$ and $|t'_v|$, $(-1)^{\nu_3} = \Pi_v \xi_v(\pi)$ depends on both magnitudes and signs of t_v and t'_v. Evidently, then, if Dirac valleys are present at these $\boldsymbol{k}_{||}$, the superlattice valley engineering (*c.f.* Eq. (1)) will be a powerful mechanism for creating WTIs. It may be noted that for a TCI, the topological numbers of time-reversal symmetry $\nu_\alpha = 0$ for $\alpha = 0, 1, 2, 3$. The topological number (e.g., mirror Chern number) that characterizes the TCI materials is defined with respect to crystal's geometric symmetry[6,7]. The above analysis suggests a unifying pathway to tailor-make three different classes of TIs through *valley-dependent* interfacial state dimerization. Note that this mechanism is established in the binary superlattice bearing *multiple symmetry-unrelated* interfacial Dirac states, in contrast to the superlattice with single interfacial state or multiple symmetry-equivalent interfacial states[17,18].

Having established "superlattice valley engineering" as a mechanism for creating various topological phases, in what follows, we present a concrete demonstration using the unique interfacial states of tin telluride (SnTe). SnTe class of TCI has been successfully prepared experimentally[19–21], and very importantly, its superlattices is readily achievable[22,23]. SnTe has the sodium chloride structure and (110)-like mirror symmetries. Band inversions occur near the four inequivalent L points, as shown in Fig. 2a, giving rise to multiple nonzero mirror Chern numbers[7]. Consequently, an even number of Dirac surface states appear on any surface[19–21] or interface that preserves a (110)-like mirror symmetry. We will focus on the [111] and [110] superlattices that harbor symmetry-distinct valleys. Without introducing strain, a [001] superlattice will not have the valley-contrasting physics, as the two Dirac interfacial states of [001] superlattice are related by mirror symmetry[18].

The [111] superlattice of SnTe with a normal insulator is particularly interesting, because in this case all the TRI points of the superlattice are derived from the interfacial Dirac valleys, as explained in Fig. 2a. The parity analysis at three M_j points are identical, and likewise at three M'_j points, as long as the $\hat{C}_3$ symmetry along the [111] direction is unbroken. The topological class of the [111] superlattice of SnTe follows readily from our arguments below Eq. (3). The

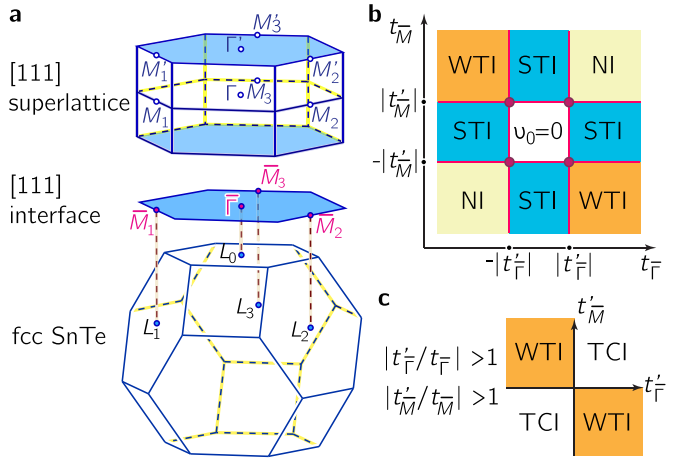

Figure 2 | Valley-dependent interfacial Dirac state dimerization in [111] superlattice of SnTe TCI. (a). Brillouin zone projection in [111] direction. (b). Topological phase diagram of the superlattice. For a [111] interface of SnTe with a NI, the Dirac nodes are located at $\bar{\Gamma}$ and $\bar{M}_j(j=1,2,3)$ on the surface Brillouin zone. Extending to the superlattice, each valley branches out into a doublet at $k_z = 0$ and π, namely, Γ, Γ' and M_j, M_j'. (c). The v_0 square in the center of b.

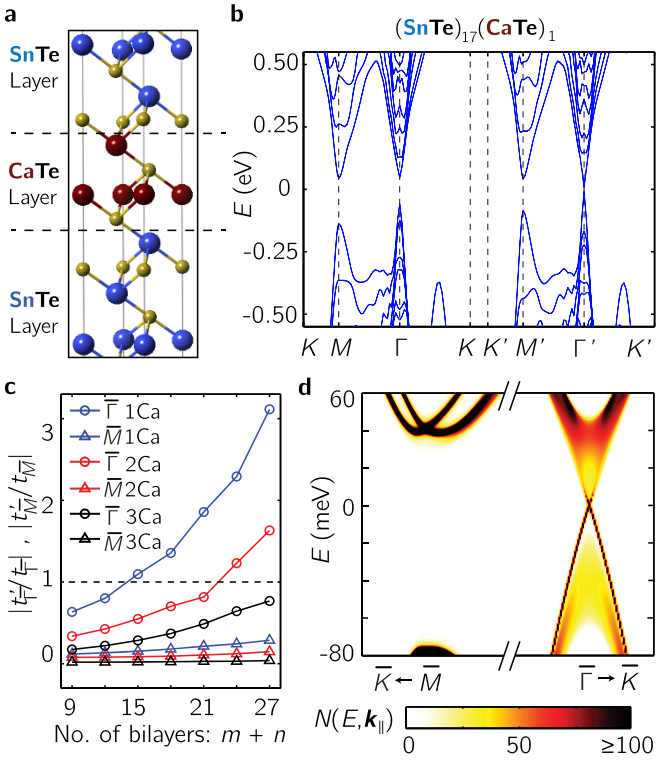

Figure 3 | Geometric and electronic structure of [111] superlattice. (a). A representative structure of $(m, 2)_{[111]}$ superlattice. Only a section of the superlattice near the interface is shown. The blue, red and yellow balls correspond to Sn, Ca and Te, respectively. (b). The band structure near the band gap of $(17, 1)_{[111]}$ superlattice. The chemical potential is set to zero energy. (c). The values of $|t'/t|$ as a function of the thickness of superlattice, at $\bar{\Gamma}$ and $\bar{M}$ valleys. Blue, red and black curves correspond to $n = 1, 2$ and 3, respectively. (d). The energy dispersion at the top surface of the semi-infinite $(17, 1)_{[111]}$ superlattice, computed as the imaginary part of the surface Green's function (see Methods). The darkness of the color corresponds to magnitude of spectral density of states $N(E, \boldsymbol{k}_{\parallel})$. The energy level of Dirac point at $\bar{\Gamma}$ is set to zero.

phase diagram is plotted in Fig. 2b and c. As we can see in the $t_{\bar{\Gamma}}$-$t_{\bar{M}}$ parameter space, three topological phases — the strong, the weak, and the crystalline — can all be created in such superlattices.

As anticipated, when $\delta_{\bar{\Gamma}}\delta_{\bar{M}} = -1$, the resulting superlattice is a STI. When $|t'/t| < 1$ or $|t'/t| > 1$ for both $\bar{\Gamma}$ and $\bar{M}$ valleys, the superlattice has an overall $v_0 = 0$. Specifically, the band topology depends on the relative signs of $t_{\bar{\Gamma}}$ and $t_{\bar{M}}$ for $|t'/t| < 1$ in both valleys, where the superlattice can be either WTI with v_0; $(v_1v_2v_3) = 0$; (001) ($t_{\bar{\Gamma}}t_{\bar{M}} < 0$) or a trivial insulator ($t_{\bar{\Gamma}}t_{\bar{M}} > 0$). When $|t'/t| > 1$ in both valleys, the classification depends on the signs of $t'_{\bar{\Gamma}}$ and $t'_{\bar{M}}$, where the superlattice can be either WTI with v_0; $(v_1v_2v_3) = 0$; (001) ($t'_{\bar{\Gamma}}t'_{\bar{M}} < 0$) or congener TCI ($t'_{\bar{\Gamma}}t'_{\bar{M}} > 0$) (Fig. 2c). It is worth remarking that the points where $|t'/t| = 1$ for both $\bar{\Gamma}$ and $\bar{M}$ (the red circles in Fig. 2b), are *topological tetracritical points*[24], which reflect the simultaneous presence of topological order of two distinct valleys. It may also be deduced that a finite neighbourhood of the phase boundaries is metallic via electron-hole compensation between valleys.

The valley engineering proposed above can only be established with judicious materials design. We employ density-functional theory simulations to study the superlattices of SnTe[25,26]. Computational details can be found in the section Methods. We choose the isostructural calcium telluride (CaTe) for the spacer layer, instead of the obvious choice of isovalent IV-VI semiconductors, PbTe and GeTe, for two reasons. First, the lattice mismatch between SnTe and CaTe is less than 1%, a feature conducive to experimental growth of heterostructures. Besides, the lattice matching avoids strain-induced topological phase transitions of SnTe and the spacer layer (e.g. PbTe)[7]. Second, GeTe is known to undergo ferroelectric distortion[27], which, albeit interesting in itself in the context valley engineering, unduly complicates a first analysis. CaTe is a normal insulator with a computed gap of 1.3 eV. SnTe has 107 meV direct gaps at L, agreeing with previous work[7]. A [111] superlattices composed of m SnTe bilayers and n CaTe bilayers is denoted $(m, n)_{[111]}$ for brevity. A representative structure of $(m, 2)_{[111]}$ superlattice is shown in Fig. 3a. Inversion symmetry is present in all superlattices considered after structural optimization.

Our calculations examine $(m, n)_{[111]}$ with a single, double and triple bilayer of the normal insulator CaTe ($n = 1, 2, 3$), with total number of bilayers up to $m + n = 27$. A representative band structure for $(17, 1)_{[111]}$ superlattice is shown in Fig. 3b, with direct band gaps at Γ, Γ', M and M'. Based on the direct gaps of the Kohn-Sham states at the TRI points in relation to Hamiltonian (1), we estimate the $|t|$ and $|t'|$ at $\bar{\Gamma}$ and $\bar{M}$. We take $4|t| = |\Delta(0) + \Delta(\pi)|$ and $4|t'| = |\Delta(0) - \Delta(\pi)|$. Here, Δ is the band gap, which can be negative after band inversion, at $k_z = 0, \pi$ of a given valley.

The crucial observation is that for $n = 1$, $|t'|$ surpasses $|t|$ at $\bar{\Gamma}$ valley for $m \geq 14$. When $n = 2$, similar switch of hopping strengths occurs for $m \geq 22$. In contrast, for the superlattice series considered, the thickness of SnTe layer is insufficient to cause switch at $\bar{M}$. We then expect that the [111] superlattice becomes a STI from NI when $m \geq 14$ ($m \geq 22$) for $n = 1$ ($n = 2$). Indeed, this expectation is confirmed by computing $\mathcal{Z}_2$ invariant v_0 from the parities of Kohn-Sham wavefunctions, as shown in Supplementary Information (S.I. hereafter). The value of v_0 becomes 1 from 0, as the thickness of SnTe layer is beyond the thresholds. Complementarily, Fig. 3d shows the energy dispersion of surface states located at the top surface of the semi-infinite $(17, 1)_{[111]}$ superlattice, which is directly accessible experimentally (e.g. by ARPES). Consistent with the result that bulk $v_0 = 1$, there is only one Dirac cone around $\bar{\Gamma}$ within the bulk gap. Moreover, because Fig. 2b remains unchanged when the signs of $t_{\bar{\Gamma}}$ and $t_{\bar{M}}$ are switched simultaneously, their overall signs can not be determined. However, according to the aforementioned topological quantum phase transition from a NI to a STI, we can conclude that $t_{\bar{\Gamma}}$ and $t_{\bar{M}}$ have the same sign. For superlattices with triple CaTe bilayer ($n = 3$, $m \leq 24$), $\mathcal{Z}_2$ indices show that they stay topologically trivial,

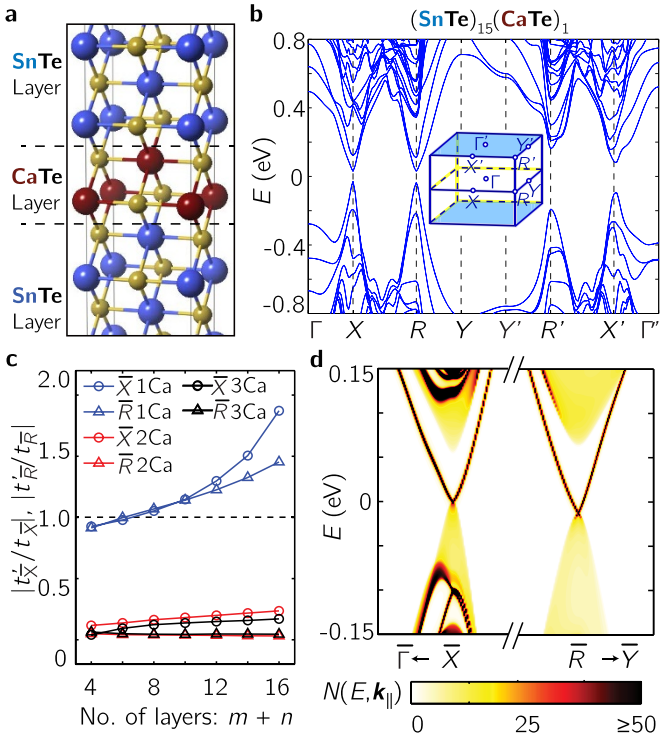

Figure 4 | Geometric and electronic structure of [110] superlattice. (a). A representative structure of $(m, 2)_{[110]}$ superlattice. (b). A representative band structure near the band gap of $(15, 1)_{[110]}$ superlattice. The inset shows the Brillouin zone. (c). The values of $|t'/t|$ as a function of the thickness of superlattice, at $\bar{X}$ and $\bar{R}$. Blue, red and black curves correspond to $n = 1, 2$ and 3. (d). The energy dispersion at the top surface of the semi-infinite $(15, 1)_{[110]}$ superlattice. The energy level of Dirac point at $\bar{X}$ is set to zero.

agreeing with the observation from Fig. 3c that there is no band inversion with the thickness of SnTe layers considered.

We next consider a series of [110] superlattices with a single, double and triple layer of CaTe (Fig. 4a). In the projected Brillouin zone along [110] direction, there are two symmetry-distinct Dirac valleys at $\bar{X}(\pi,0)$ and $\bar{R}(\pi,\pi)$, respectively. Therefore, the [110] superlattices show direct band gaps at X, X', R, R' (Fig. 4b). In contrast with [111] supelattices, not all TRI points of [110] superlattices can be derived from interfacial Dirac valleys. However, it is still possible to design various topological insulators by tuning t and t' at $\bar{X}$ and $\bar{R}$ valleys of [110] superlattices. As shown in Fig. 4c, for $n = 1$, band inversion occurs at both $\bar{X}$ and $\bar{R}$ valleys when $m \geq 7$. Based on the calculation of the $\mathcal{Z}_2$ invariant, the $(m, 1)_{[110]}$ superlattices become a WTI (see S.I.). When $m + n = 8$, 12 and 16, the $\mathcal{Z}_2$ indices are ν_0; $(\nu_1\nu_2\nu_3) = 0$; (0, 1, 0). When $m + n = 10$ and 14, the indices are 0;(0, 1, 1). The energy dispersion at the top surface of the semi-infinite $(15, 1)_{[110]}$ superlattice shows that two symmetry-unrelated Dirac cones appear around both $\bar{X}$ and $\bar{R}$ within the bulk gap, agreeing with its $\mathcal{Z}_2$ indices (Fig. 4d). In contrast, in the superlattices with $n = 2$ and 3, no phase transition is seen in the models calculated. It is noteworthy that the WTI phase of the [110] superlattice will have two symmetry-unrelated valleys (the topological surface states) on its top surface, which is very important for direct experimental measurement and device making. This is to be compared with the WTIs based on layered stacking of quantum spin Hall insulators[9,28,29] and the ones in [111] superlattices of SnTe TCI with ν_0; $(\nu_1\nu_2\nu_3) = 0$; (0, 0, 1), of which the topological surface states are located on side surfaces[5].

The SnTe/CaTe models have only uncovered a small region of the rich phase diagrams, such as Figs. 2b–c. The identification of possible topological phases beyond the current system may be sought profitably in the spacer material, which plays the critical role as a mediator and modulator in valley-dependent couplings. The tunability of coupling through the spacer can be elucidated based on a perturbation theory,

$$t'_v \approx -\frac{1}{2}\sum_k \left[\frac{1}{E_{vk}-E_{v+}} + \frac{1}{E_{vk}-E_{v-}}\right] \check{t}_{+k}\check{t}_{k-}, \qquad (4)$$

to second order, where $E_{vk} - E_{v\tau_z}$ is the energy difference between the kth state of the spacer layer and the Dirac valley (v, τ_z), and $\check{t}_{kv}$ is the corresponding hopping amplitude. A pair of Dirac states ($\tau_z = \pm$) may now be non-degenerate with a ferroelectric spacer[27]. Evidently, variation of the band gap of spacer layer and its energy level alignment with the Dirac points will enable high tunability of both the magnitude and sign of t'_v. This can be achieved through material choice. More interestingly, the level alignment can be changed through *in situ* external gating, which may become an efficient experimental knob to tune the phase transitions in Figs. 2b–c.

It is clear that valley-dependent dimerization of Dirac interfacial states can be a powerful mechanism to design topological phases, out of a binary superlattice. This mechanism is rather generic, and applies to any system with multiple band inversions and Dirac interfacial states, such as TCI, WTI and, quite possibly, elemental bismuth[4–7]. This strategy can also be made useful in valleytronics[30–32]. Yang et al recently predicted that a WTI could be fabricated from the [001] superlattice of SnTe and PbTe, which has two symmetry-equivalent surface Dirac points[18]. In comparison, the two surface valleys of the [110]-superlattice WTI proposed here are unrelated by any symmetry, a crucial observation that entails rich possibilities for novel valley-based devices, such as valley valve and filter[33], by juxtaposition of heterostructures with massless and massive valleys tailored with the proposed mechanism. Elastic strain engineering will also find important applications here, where deformation can reversibly break the symmetry that relates a subset of valleys[34]. Finally, the ability to tune the number of Dirac surface states is especially attractive in the pursuit of exotic quantum anomalous Hall effects[15,35], Weyl semimetals[17,36], and topological superconductors[10].

Methods

We use first-principle density functional theory calculations to investigate the atomic and electronic structure of [111] and [110] superlattice of SnTe/CaTe. The Perdew-Burke-Ernzerhof exchange-correlation functional and the projector-augmented wave potentials are used, as implemented in the Vienna *ab initio* Simulation Package (VASP)[25,26]. A plane-wave cutoff of 350 eV is adopted. We use a k-mesh of $7 \times 7 \times 2$ for [111] superlattices, and a **k**-mesh of $5 \times 7 \times l$ ($l \geq 3$) for [110] superlattices, where l depends on the thickness of [110] superlattices. The valence includes 4 electrons for Sn ($5s^25p^2$), 10 for Ca ($3s^23p^64s^2$) and 6 for Te ($5s^25p^4$). Structure optimizations are performed with a convergence threshold of 0.01 eV/Å on the interatomic forces. To obtain the surface states of topological superlattices, we construct the surface Greens function of the semi-infinite superlattice, using Wannier functions and corresponding hopping parameters from the *ab initio* calculation. And then, the spectral density of states $N(E, \boldsymbol{k}_{||})$ at the surface can be obtained from the imaginary part of the surface Green's function, which shows the energy dispersion of surface states[37–39]. Here, the spectral density of states is the function of the energy E and the parallel momentum $\boldsymbol{k}_{||}$.

1. Hasan, M. Z. & Kane, C. L. *Colloquium*: Topological insulators. *Rev. Mod. Phys.* **82**, 3045–3067 (2010).
2. Qi, X.-L. & Zhang, S.-C. Topological insulators and superconductors. *Rev. Mod. Phys.* **83**, 1057–1110 (2011).
3. Moore, J. E. The birth of topological insulators. *Nature* **464**, 194–198 (2010).
4. Fu, L. & Kane, C. L. Time reversal polarization and a Z_2 adiabatic spin pump. *Phys. Rev. B* **74**, 195312 (2006).
5. Fu, L. & Kane, C. L. Topological insulators with inversion symmetry. *Phys. Rev. B* **76**, 045302 (2007).
6. Fu, L. Topological crystalline insulators. *Phys. Rev. Lett.* **106**, 106802 (2011).
7. Hsieh, T. H. *et al.* Topological crystalline insulators in the SnTe material class. *Nat. Commun.* **3**, 982 (2012).
8. Kargarian, M. & Fiete, G. A. Topological crystalline insulators in transition metal oxides. *Phys. Rev. Lett.* **110**, 156403 (2013).

9. Rasche, B. *et al*. Stacked topological insulator built from bismuth-based graphene sheet analogues. *Nat. Mater.* **12**, 422–425 (2013).
10. Fu, L. & Kane, C. L. Superconducting proximity effect and majorana fermions at the surface of a topological insulator. *Phys. Rev. Lett.* **100**, 096407 (2008).
11. Yu, R. *et al*. Quantized anomalous Hall effect in magnetic topological insulators. *Science* **329**, 61–64 (2010).
12. Chang, C.-Z. *et al*. Experimental observation of the quantum anomalous Hall effect in a magnetic topological insulator. *Science* **340**, 167–170 (2013).
13. Xiao, D., Zhu, W., Ran, Y., Nagaosa, N. & Okamoto, S. Interface engineering of quantum Hall effects in digital transition metal oxide heterostructures. *Nat. Commun.* **2**, 596 (2011).
14. Rüegg, A. & Fiete, G. A. Topological insulators from complex orbital order in transition-metal oxides heterostructures. *Phys. Rev. B* **84**, 201103 (2011).
15. Cai, T.-Y. *et al*. Emergent topological and half semimetallic Dirac Fermions at oxide interfaces. *arxiv*,1310.2471 (2013).
16. Su, W. P., Schrieffer, J. R. & Heeger, A. J. Solitons in Polyacetylene. *Phys. Rev. Lett.* **42**, 1698–1701 (1979).
17. Burkov, A. A. & Balents, L. Weyl semimetal in a topological insulator multilayer. *Phys. Rev. Lett.* **107**, 127205 (2011).
18. Yang, G., Liu, J., Fu, L., Duan, W. & Liu, C. Weak topological insulators in PbTe/SnTe superlattices. *Phys. Rev. B* **89**, 085312 (2014).
19. Tanaka, Y. *et al*. Experimental realization of a topological crystalline insulator in SnTe. *Nat. Phys.* **8**, 800–803 (2012).
20. Dziawa, P. *et al*. Topological crystalline insulator states in $Pb_{1-x}Sn_xSe$. *Nat. Mater.* **11**, 1023–1027 (2012).
21. Xu, S.-Y. *et al*. Observation of a topological crystalline insulator phase and topological phase transition in $Pb_{1-x}Sn_xTe$. *Nat. Commun.* **3**, 1192 (2012).
22. Ishida, A. *et al*. Electrical and thermoelectrical properties of SnTe-based films and superlattices. *Appl. Phys. Lett.* **95**, – (2009).
23. Ishida, A., Yamada, T., Tsuchiya, T., Inoue, Y. & Kita, T. Semimetallic properties of SnTe/PbSe type-II superlattices. *Phys. Procedia* **3**, 1295–1298 (2010).
24. Fisher, M. E. & Nelson, D. R. Spin flop, supersolids, and bicritical and tetracritical points. *Phys. Rev. Lett.* **32**, 1350–1353 (1974).
25. Perdew, J. P., Burke, K. & Ernzerhof, M. Generalized gradient approximation made simple. *Phys. Rev. Lett.* **77**, 3865–3868 (1996).
26. Kresse, G. & Joubert, D. From ultrasoft pseudopotentials to the projector augmented-wave method. *Phys. Rev. B* **59**, 1758–1775 (1999).
27. Pawley, G. S., Cochran, W., Cowley, R. A. & Dolling, G. Diatomic ferroelectrics. *Phys. Rev. Lett.* **17**, 753–755 (1966).
28. Yan, B., Müchler, L. & Felser, C. Prediction of weak topological insulators in layered semiconductors. *Phys. Rev. Lett.* **109**, 116406 (2012).
29. Tang, P. *et al*. Weak topological insulators induced by the interlayer coupling: A first-principles study of stacked Bi_2TeI. *Phys. Rev. B* **89**, 041409 (2014).
30. Cao, T. *et al*. Valley-selective circular dichroism of monolayer molybdenum disulphide. *Nat. Commun.* **3**, 887 (2012).
31. Xiao, D., Liu, G.-B., Feng, W., Xu, X. & Yao, W. Coupled spin and valley physics in monolayers of MoS_2 and other group-VI dichalcogenides. *Phys. Rev. Lett.* **108**, 196802 (2012).
32. Li, X., Cao, T., Niu, Q., Shi, J. & Feng, J. Coupling the valley degree of freedom to antiferromagnetic order. *Proc. Natl. Acad. Sci. USA* **110**, 3738–3742 (2013).
33. Jiang, H., Liu, H., Feng, J., Sun, Q. & Xie, X. C. Transport discovery of emerging robust helical surface states in Z_2 systems. *arxiv*,1403.3743 (2014).
34. Fang, C., Gilbert, M. J. & Bernevig, B. A. Large Chern number quantum anomalous Hall effect in thin-film topological crystalline insulators. *arxiv*,1306.0888 (2013).
35. Zhang, F., Li, X., Feng, J., Kane, C. L. & Mele, E. J. Zeeman field-tuned transitions for surface chern insulators. *arXiv*,1309.7682 (2013).
36. Wan, X., Turner, A. M., Vishwanath, A. & Savrasov, S. Y. Topological semimetal and Fermi-arc surface states in the electronic structure of pyrochlore iridates. *Phys. Rev. B* **83**, 205101 (2011).
37. Marzari, N. & Vanderbilt, D. Maximally localized generalized Wannier functions for composite energy bands. *Phys. Rev. B* **56**, 12847–12865 (1997).
38. Souza, I., Marzari, N. & Vanderbilt, D. Maximally localized Wannier functions for entangled energy bands. *Phys. Rev. B* **65**, 035109 (2001).
39. Sancho, M. L., Sancho, J. L. & Rubio, J. Quick iterative scheme for the calculation of transfer matrices: application to Mo (100). *J. Phys. F: Met. Phys.* **14**, 1205 (1984).

Acknowledgments

J.F. is supported by the National Natural Science Foundation of China (NSFC No.11174009) and China 973 Program (No.2013CB921900 and No.2011CBA00109). Q.N. is supported by NBRPC (No. 2012CB921300 and No. 2013CB921900), and NSFC (No.91121004). F.Z. has been supported by UT Dallas research enhancement funds. We thank Profs. Junren Shi and Fa Wang for useful discussions.

Author contributions

X.L. performed the DFT calculations. X.L., J.F., F.Z. and Q.N. analyzed the data and wrote the paper. J.F. designed and coordinated the project.

Additional information

Supplementary information accompanies this paper at http://www.nature.com/scientificreports

Competing financial interests: The authors declare no competing financial interests.

How to cite this article: Li, X., Zhang, F., Niu, Q. & Feng, J. Superlattice valley engineering for designer topological insulators. *Sci. Rep.* **4**, 6397; DOI:10.1038/srep06397 (2014).